

## MIT Open Access Articles

*Maximizing Hysteretic Losses in Magnetic Ferrite Nanoparticles via Model-Driven Synthesis and Materials Optimization*

The MIT Faculty has made this article openly available. **Please share** how this access benefits you. Your story matters.

**Citation:** Chen, Ritchie, Michael G. Christiansen, and Polina Anikeeva. "Maximizing Hysteretic Losses in Magnetic Ferrite Nanoparticles via Model-Driven Synthesis and Materials Optimization." ACS Nano 7, no. 10 (October 22, 2013): 8990–9000.

**As Published:** <http://dx.doi.org/10.1021/nn4035266>

**Publisher:** American Chemical Society (ACS)

**Persistent URL:** <http://hdl.handle.net/1721.1/92978>

**Version:** Author's final manuscript: final author's manuscript post peer review, without publisher's formatting or copy editing

**Terms of Use:** Article is made available in accordance with the publisher's policy and may be subject to US copyright law. Please refer to the publisher's site for terms of use.



# Maximizing Hysteretic Losses in Magnetic Ferrite Nanoparticles *via* Model-Driven Synthesis and Materials Optimization

*Ritchie Chen,<sup>1</sup> Michael G. Christiansen,<sup>1</sup> and Polina Anikeeva<sup>1, 2\*</sup>*

<sup>1</sup>Department of Materials Science and Engineering, Massachusetts Institute of Technology,  
Cambridge, MA 02139, (USA)

<sup>2</sup>Research Laboratory of Electronics, Massachusetts Institute of Technology,  
Cambridge, MA 02139, (USA)

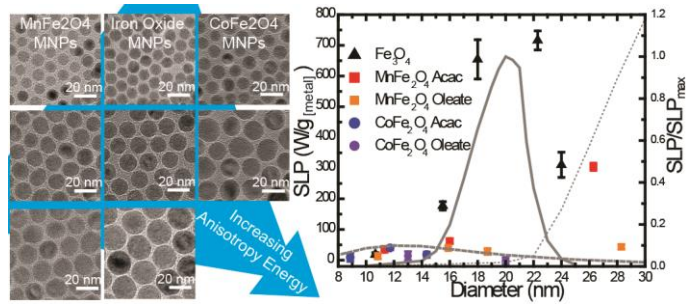
\* Address correspondence to [anikeeva@mit.edu](mailto:anikeeva@mit.edu)

## ABSTRACT

This article develops a set of design guidelines for maximizing heat dissipation characteristics of magnetic ferrite  $MFe_2O_4$  ( $M = Mn, Fe, Co$ ) nanoparticles in alternating magnetic fields. Using magnetic and structural nanoparticle characterization, we identify key synthetic parameters in the thermal decomposition of organometallic precursors that yield optimized magnetic nanoparticles over a wide range of sizes and compositions. The developed synthetic procedures allow for gram-scale production of magnetic nanoparticles stable in physiological buffer for several months. Our magnetic nanoparticles display some of the highest heat dissipation rates, which are in qualitative agreement with the trends predicted by a dynamic hysteresis model of coherent magnetization reversal in single domain magnetic particles. By combining physical simulations with robust scalable synthesis and materials characterization techniques, this work provides a pathway to a model-driven design of magnetic nanoparticles tailored to a variety of biomedical applications ranging from cancer hyperthermia to remote control of gene expression.

**Key Words:** magnetic nanoparticles · magnetic hyperthermia · anisotropy energy · organometallic decomposition · water-soluble nanoparticles · large-scale synthesis

## TABLE OF CONTENTS (TOC) GRAPHIC



The ability to tune the materials properties of magnetic nanoparticles (MNPs) composed of spinel ferrites  $MFe_2O_4$  ( $M = Mn, Fe, Co$ ) enables a variety of biomedical applications.<sup>1-3</sup> For example, achieving a high magnetic moment is essential for effective magnetic resonance imaging (MRI) contrast agents, whereas maximizing power dissipation in alternating magnetic fields (AMF) is desirable for heat-induced necrosis of tumor tissues.<sup>4,5</sup> Recent work demonstrating fine control over the size, shape, composition, and surface passivation of superparamagnetic MNPs has propelled the latter method, magnetic hyperthermia, into clinical trials.<sup>6</sup> AMF-induced heat dissipation in MNPs has also found new applications in remote control of cellular signaling and gene transcription *in vivo*.<sup>7,8</sup>

For therapeutic purposes, the MNPs must be administered at the lowest concentrations possible, and the product of AMF frequency  $f$  and amplitude  $H_0$  should be less than  $5 \times 10^9 \text{ A} \cdot \text{m}^{-1} \cdot \text{s}^{-1}$ , a figure of merit intended to limit non-specific heating of healthy tissue *via* eddy currents induced by the applied AMF.<sup>9</sup> As a result, the field parameters are usually limited to amplitudes 5 - 20  $\text{kA} \cdot \text{m}^{-1}$  and frequencies below 1 MHz. In order to achieve the desired therapeutic effect under the field frequency product constraint, the MNP power dissipation rate per gram, or specific loss power (SLP), has to be optimized. Because the hysteresis losses in MNPs depend on their saturation magnetization ( $M_s$ ) and the effective anisotropy energy barrier, these two parameters can be varied for SLP optimization for an AMF of a given amplitude and frequency. Guided by the physical model of coherent magnetization reversal in single domain MNPs, this article correlates the structural and magnetic properties of ferrite MNPs ( $MFe_2O_4$ ,  $M = Mn, Fe, Co$ ) to key synthetic parameters that determine the MNP performance as heat dissipation agents.<sup>10,11</sup> The synthetic procedures developed within this study are easily scalable to production of gram scale quantities of monodisperse MNPs with anisotropy energies varying

over 3 orders of magnitude in a size range of 8 - 28 nm stable in physiological buffers for several months. We experimentally observe some of the highest SLP values reported to date at a given AMF amplitude and frequency, which are in qualitative agreement with a generalized physical model of hysteretic power dissipation that can be used for the simulation-driven design of MNPs tailored for a specific biomedical application.

## **THEORETICAL BASIS**

A MNP ensemble dissipates heat when magnetic moments of individual MNPs overcome an anisotropy energy barrier to realign with an applied field to reduce their configurational energy. While spinel ferrites have cubic anisotropy in their bulk form, this work assumes an effective uniaxial symmetry due to surface effects that introduce multiple sublattices on the surface of MNPs at the nanoscale.<sup>6,12</sup> As an estimate, the effective uniaxial anisotropy energy constant ( $K_{eff}$ ) was taken to be approximately equal to the absolute value of the first order cubic magnetocrystalline anisotropy constant  $K_1$ . The transition of moments over the barrier is thermally activated, so that the expected power dissipation depends not only on the amplitude of the applied field's perturbation to the anisotropy energy landscape, but also the ambient temperature and cyclic timescale of the perturbation. At a field magnitude determined ideally by the materials' saturation magnetization and the effective anisotropy energy, the barrier to coherent reversal vanishes for uniaxial MNPs. This critical field magnitude might be called the zero temperature coercive field, though it should be understood that this terminology neglects the temperature dependence of  $K_1$ , and thus will not reflect the coercive field actually observed near 0 K.<sup>13</sup> By considering the relative magnitude of the applied field to the zero temperature

coercive field, the hysteretic power dissipation of MNPs can be conveniently divided into several regimes.

At field amplitudes well below the coercive field, the barrier is not significantly perturbed and the magnetization of the MNP ensemble scales linearly with the applied field. In this regime, hysteretic losses can be appropriately modeled with linear response theory (LRT), such as the frequently cited treatment by Rosensweig.<sup>14</sup> In that work, coherent magnetization reversal (“Neél relaxation”) was considered in the context of an unperturbed and stochastic magnetization reversal, with the implication that physical rotation of the particle must dominate for maximal heat dissipation. However, it has been experimentally demonstrated that increasing the viscosity of the fluid surrounding MNPs did not dramatically alter their SLPs, indicating that magnetization reversal can lead to significant heating.<sup>15</sup> Field amplitudes commonly used for therapeutic purposes may significantly perturb the anisotropy barrier, particularly for materials with low anisotropy energy density values (*i.e.*,  $\text{MnFe}_2\text{O}_4$ ,  $K_{\text{eff}} = 3.0 \times 10^3 \text{ J m}^{-3}$  or  $\text{Fe}_3\text{O}_4$ ,  $K_{\text{eff}} = 1.4 \times 10^4 \text{ J m}^{-3}$ ). At sufficiently high applied fields, the material approaches saturation and should no longer be expected to respond linearly. As a result, SLP values cannot be made arbitrarily large by increasing the field amplitude and frequency, as predicted by the functional form of LRT. Thus at therapeutically relevant field amplitudes, well-motivated use of LRT-based calculations is limited to materials with comparatively high anisotropy energy, such as  $\text{CoFe}_2\text{O}_4$  ( $K_{\text{eff}} = 2.0 \times 10^5 \text{ J m}^{-3}$ ). Assuming that MNPs with coercive fields much higher than the applied field are able to rotate freely, the majority of the hysteretic loss is attributable to frictional heat generated by the rotation of the particle in the medium.<sup>15</sup>

In the limit of field amplitudes larger than the coercive field, the shape and area of the resulting hysteresis loops approaches, but does not exceed the theoretical limit for uniaxial single-domain

MNPs described by the Stoner-Wohlfarth model at 0 K.<sup>16</sup> In order to take into account thermal activation and perturbative timescale, an effective  $H_C$  can be considered to vary with AMF frequency as well as the temperature of the environment.<sup>17</sup>

In the intermediate regime, when the AMF amplitude is less than the coercive field but still perturbs the barrier significantly, a numerical method is required to effectively model the SLP. We adopted the model by Carrey *et al.* to calculate the hysteresis loops for a set of ferrite materials at these conditions for MNPs with diameters between 5-30 nm.<sup>10</sup> This model employs a “macrospin” approximation that assumes moments are confined to local energy minima. Frictional losses from Brownian rotation are not considered because they do not contribute significantly to heat dissipation for the range of MNP sizes explored in this paper.

To illustrate the origin of heat dissipation in MNPs, we first calculate hysteresis loops for magnetite  $\text{Fe}_3\text{O}_4$  with varying diameters with applied AMFs at amplitude  $H_0 = 15 \text{ kA m}^{-1}$  and frequency  $f = 500 \text{ kHz}$  (**Figure 1A**). We assume that the MNPs are effectively uniaxial, their easy-axes aligned with the applied field, and that the attempt rate is constant at  $10^{10} \text{ Hz}$ . Due to surface effects, an effective uniaxial anisotropy is assumed for ferrite MNPs as long as the remanent to saturation magnetization ratio is less than 0.5, which can be experimentally determined.<sup>18</sup> These assumptions are made primarily for convenience and are expected to overestimate SLP values while making reasonable qualitative predictions. Neither perfect alignment nor random alignment are well motivated assumptions for MNPs that can freely rotate, and the actual behavior would likely involve intermediate correlation and vary with the effective anisotropy energy of the MNP relative to the ambient thermal energy.<sup>10</sup> For MNPs with diameters less than 15 nm (at  $f = 500 \text{ kHz}$ ), the hysteresis loop appears almost reversible due to the negligible anisotropy barrier for the given temperature and frequency. This



superparamagnetic behavior results in low power loss (**Figure 1B**). As the energy barrier scales with MNP volume,  $E_a \sim K_{eff} \cdot d^3$ , the area of the hysteresis loop becomes significantly larger and displays a ferromagnetic shape at diameters above 18 nm. SLP reaches its maximum value for iron oxide MNPs with 20 nm diameters, which corresponds to a hysteresis loop with the largest area at the chosen field parameters. As the MNP diameter increases beyond 20 nm, the anisotropy energy increases such that the field amplitude no longer exceeds the coercive field and only minor hysteresis loops can be accessed, leading to a decrease in overall heat dissipation.

Figure 1B summarizes the dependence of the SLP on the diameter as well as the  $K_{eff}$  value of the MNPs. Because the  $K_{eff}$  value of  $\text{CoFe}_2\text{O}_4$  is an order of magnitude greater than that of  $\text{Fe}_3\text{O}_4$ , only minor hysteresis loops are accessed at the chosen AMF amplitude. Our calculations do not account for cubic anisotropy of the ferrite material and hence does not hold for materials like  $\text{CoFe}_2\text{O}_4$  with especially large  $K_{eff}$  value. LRT was used to determine the SLP values for heat dissipation, which arises primarily from the frictional heating generated by the physical rotation of the particles when the applied field amplitude is much smaller than the coercive field. On the other hand, the  $K_{eff}$  value of  $\text{MnFe}_2\text{O}_4$  is an order of magnitude lower than that of  $\text{Fe}_3\text{O}_4$ , which results in this transition from a superparamagnetic to ferromagnetic hysteretic loss to occur at larger MNP diameters. In fact, we find that  $\text{MnFe}_2\text{O}_4$  MNPs exhibit significant hysteretic losses only at diameters greater than 22 nm.

## RESULTS AND DISCUSSION

A comprehensive palette of ferrite MNPs of varying size and composition is essential for an experimental evaluation of the predictive ability of the model illustrated in **Figure 1**. While thermal decomposition of organometallic precursors in the presence of coordinating ligands is an effective method to prepare monodisperse and uniformly shaped MNPs, achieving bulk values of

magnetic properties in a variety of MNP sizes remains a synthetic challenge.<sup>19-21</sup> To produce a wide range of ferrite MNPs, we have built upon and contrasted two major organometallic syntheses based on the thermal decomposition of metal-oleate and metal acetylacetonate (acac) precursors.<sup>20,21</sup> While thermal decomposition of metal-oleate precursors offers fine control over MNPs size and composition, the material's  $M_s$  is known to be poor as compared to bulk values, which leads to low hysteretic losses.<sup>22</sup> This is attributed to the formation of wüstite ( $\text{Fe}_{1-x}\text{O}$ , where  $x = 0.05 - 0.17$ ),<sup>23</sup> an antiferromagnetic phase that is paramagnetic at room temperature and hence does not contribute to hysteretic power dissipation in these MNPs.<sup>24</sup> In contrast, a combination of reducing and oxidizing ligands present during the thermal decomposition of metal-acac precursors yields MNPs comprising mixed  $\text{Fe}^{2+}/\text{Fe}^{3+}$  necessary for the magnetite/maghemite spinel ferrite structure.<sup>20</sup> The resulting MNPs exhibit high saturation magnetization values approaching that of bulk. However, acac-based synthesis produces MNPs below 10 nm in diameter and consequently requires a multi-step seed-mediated approach to grow shells around the MNPs in 1 nm increments. In this study, we overcome the challenges of these two synthetic routes to produce high-quality magnetic materials desirable for biomedical applications as well as essential to experimental validation of the physical model.

### **Thermal Decomposition of Metal-Oleate Precursors**

Two key modifications are introduced into the previously reported synthesis based on the thermal decomposition of metal-oleate precursors<sup>12,14</sup> to produce  $\text{MFe}_2\text{O}_4$  (where  $\text{M} = \text{Mn}, \text{Fe}, \text{or Co}$ ) with narrow size distributions and diameters tunable from 11 - 24 nm (**Figure 2**).

First, the heating rate is reduced by three times, as the previously reported heating  $3.3\text{ }^\circ\text{C min}^{-1}$  yielded slightly faceted iron oxide nanoparticles in our reaction conditions (**Figure S1**). The reduced heating rate of  $1\text{ }^\circ\text{C min}^{-1}$  yields monodisperse and spherical iron oxide MNPs with a

diameter distribution of less than 5% (**Figure 2A-D**). Similar trends are also observed in the synthesis of  $\text{MnFe}_2\text{O}_4$  and  $\text{CoFe}_2\text{O}_4$  MNPs (**Figure 2E-J**). While it has been hypothesized that nucleation and growth occur separately at 240 °C and ~300 °C respectively,<sup>21</sup> recent reports show that the transition occurs within 10 °C of each other,<sup>23</sup> and that the bulk of the homogeneous nucleation occurs above 300 °C.<sup>25,26</sup> This suggests that there is overlap between the two stages and hence reducing the heating rate allows for sufficient time for nanocrystals to nucleate and grow isotropically as the precursor fully decomposes above 300 °C.

The second modification is the use of the same solvent, 1-octadecene, for the synthesis of all MNPs. In this case, the MNP diameter is simply determined by setting the final annealing temperature between a range of 300 – 325 °C rather than choosing solvents with different boiling points. Iron oxide MNPs varying from 11 to 24 nm in diameter are synthesized when the annealing temperature is increased from 305 to 325 °C (**Figure 2A-D**). However, under identical conditions,  $\text{MnFe}_2\text{O}_4$  nanoparticles are cubic (**Figure S2A**), so the solvent amount needs to be decreased from 25 mL to 10 mL to promote supersaturated isotropic growth. In 10 mL 1-octadecene,  $\text{MnFe}_2\text{O}_4$  MNPs with diameters 10-18 nm are synthesized when the final temperature is varied between 305-325 °C (**Figure 2E-H**). Decreasing the solvent to 5 mL leads to polydisperse MNP samples. Size tuning of  $\text{CoFe}_2\text{O}_4$  MNPs using this approach is limited to  $\lesssim$  20 nm (**Figure 2I, J**) because of preferential facet growth above 310 °C.<sup>25</sup> Our simplified size tuning procedure allows for straightforward scaling of the MNP production up to gram-scale quantities (**Figure S3**). An ability to consistently produce multiple grams of monodisperse MNPs is essential for standardized biomedical experimentation as well as for future clinical applications of these materials.

## Thermal Decomposition of Metal Acetylacetonate Precursors

In addition to the metal-oleate based chemistry, we have also employed metal acetylacetonate (acac) precursors to produce tertiary ferrite MNPs (**Figure 3**). A synthetic route adapted from Sun *et al.* produces  $\text{CoFe}_2\text{O}_4$  and  $\text{MnFe}_2\text{O}_4$  MNPs of 9 nm and 7 nm in diameter respectively (**Figure 3A, D**).<sup>20</sup> This synthetic procedure requires maintaining the reaction temperature at 200 °C for 2 hours to promote nuclei formation necessary for monodispersity prior to raising the temperature to reflux. However, the prolonged nucleation period reduces the final MNP size during growth. To produce MNPs greater than 10 nm in diameter, we replace  $\text{Mn}(\text{acac})_2$  and  $\text{Co}(\text{acac})_2$  with the chloride salts  $\text{MnCl}_2$  and  $\text{CoCl}_2$  and directly heat the reaction solution to reflux at a rate of 3.3 °C/min. Because  $\text{Fe}(\text{acac})_3$  decomposes at a temperature different from  $\text{Mn}(\text{acac})_2$  and  $\text{Co}(\text{acac})_2$ ,<sup>27</sup> replacing the  $\text{Mn}^{2+}$  or  $\text{Co}^{2+}$  source with chloride salts results in direct incorporation as  $\text{Fe}(\text{acac})_3$  decomposes. These modifications yield  $\text{CoFe}_2\text{O}_4$  and  $\text{MnFe}_2\text{O}_4$  MNPs with diameters 12 nm and 11 nm respectively (**Figure 3B, E**).

As is evident from **Figure 1B**, the low magnetocrystalline anisotropy constant  $K_{eff}$  of  $\text{MnFe}_2\text{O}_4$  necessitates MNPs with diameters greater than 20 nm for appreciable SLP values to be observed. Replacing benzyl ether with a higher boiling point temperature solvent like 1-octadecene yields polydisperse samples (**Figure S4A**).<sup>28</sup> Monodisperse 16 nm MNPs are synthesized when a higher molar ratio of ligand to solvent is used in dioctyl ether (**Figure S4B**).<sup>29</sup> However, increasing the temperature in different solvents is found to be insufficient to increase the nanoparticle size above 20 nm.

While the previous seed-mediated approach can only increase the MNP diameter in 1 nm increments, resulting in cumbersome multistep procedures for MNPs of  $\leq 14$  nm in diameter,<sup>20</sup> here we developed a straightforward process allowing for 5-7 nm shell growth in a single

reaction step. By eliminating the 2 hour nucleation period and directly heating the reaction solution to reflux, we have synthesized 14 nm  $\text{CoFe}_2\text{O}_4$  and 26 nm  $\text{MnFe}_2\text{O}_4$  MNPs using seeds with diameters of 7 nm and 11 nm respectively (**Figure 3C, F**).

### **Magnetic Properties of MNPs**

We first investigated the magnetic behavior of the as-synthesized materials dispersed in toluene by measuring the field dependence of the magnetization at room temperature and at 5 K. Room temperature magnetization curves measured by vibrating sample magnetometer (VSM) indicate that the MNPs synthesized from metal-oleate precursors have low saturation magnetization  $M_s$  values comparable to the bulk material (**Table 1** and **Figure 4A**). Comparatively low  $M_s$  values for small MNPs can be attributed to the formation of a magnetically frustrated surface layer due to incomplete coordination of metal ions. This effect typically becomes less significant leading to increased  $M_s$  with increasing MNP diameter.<sup>30</sup> Surprisingly, MNPs synthesized *via* the metal-oleate based route exhibit further decrease in  $M_s$  with increasing particle size. Saturation magnetization values for iron oxide MNPs fall from  $\sim 35 \text{ emu g}^{-1}$  to less than  $20 \text{ emu g}^{-1}$  for MNP diameters increasing from 5 nm to 22 nm.<sup>21</sup> To further investigate the decrease of the  $M_s$  with MNP size, we calculate the magnetic volume, a proxy for the magnetic moment that assumes bulk saturation magnetization of the magnetized material, from room temperature magnetization curves using a linear fit for static magnetic susceptibility in the low field limit.<sup>10</sup> The behavior of randomly oriented particles converges on the Langevin function in the limit of low fields regardless of their anisotropy energy.<sup>10</sup> We find that the as-synthesized magnetic diameter of these MNPs never increases beyond 10 nm despite a larger measured physical diameter (**Table 1** and **Figure 4B**). Similarly, for the ternary metal oxides, the measured saturation magnetization

also decreases with increasing MNP size from 54 to 31  $\text{emu g}^{-1}$  for  $\text{MnFe}_2\text{O}_4$  and 15 to 3  $\text{emu g}^{-1}$  for  $\text{CoFe}_2\text{O}_4$  MNPs.

Furthermore, the as-synthesized MNPs do not exhibit saturation even at high fields, suggesting the presence of a paramagnetic-like phase (**Figure 5A**). The inset in **Figure 5A** details the field-dependent magnetization at low fields and presents evidence of exchange-bias, which not only arises in compositionally hybrid structures but also at order-disorder interphases.<sup>31</sup> The example hysteresis curves of as synthesized 18 nm iron oxide and 11 nm  $\text{MnFe}_2\text{O}_4$  MNPs display a shift towards negative fields by 1300 Oe and 850 Oe respectively. Because the characteristic length for exchange bias is on the order of 1-2 nm nanometers,<sup>32</sup> the observed shifts cannot be attributed to dipole-dipole interactions between particles with different magnetic phases. As the size of the MNP increases, the decreasing magnetic diameter indicates that less than 20% of the volume fraction of the MNP is ferromagnetic, suggesting heterogeneity within the as-synthesized MNPs (**Table 1**). Levy *et al.* have shown that regions of structural disorder in their iron oxide nanoparticles contribute to this effect since the moments of the magnetically frustrated phases do not fully align even at high field.<sup>33</sup> The observed exchange bias in these samples indicates that a ferromagnetic and an antiferromagnetic phase are in intimate contact.<sup>34</sup>

While Levy *et al.* attribute the magnetically frustrated phases to strain in the crystal structure of their MNPs, the observed exchange bias, paramagnetic-like susceptibility, and small magnetic cores of our MNPs suggest instead the presence of a wüstite phase. Powder x-ray diffraction (XRD) studies clearly demonstrate the presence of both wüstite and magnetite/maghemite phases, with the (111), (200), (220), (311), and (222) peaks from the wüstite fcc structure clearly identified (**Figure 6A**). Wüstite has been observed as an intermediary species when the synthesis environment is not sufficiently oxidizing to form maghemite or magnetite phases,

which is characteristic of thermal decomposition of metal-oleate precursors.<sup>23,35,36</sup> At the nanoscale, the magnetization of wüstite phase does not saturate even at high fields at 5 K.<sup>24</sup> Combined with evidence from literature, our data suggests that the MNP samples may be comprised of a spinel-like phase coherently embedded in a wüstite matrix. Because wüstite is a metastable phase, conversion to magnetite can be readily achieved under certain conditions.<sup>22,35</sup> The diameters of MNPs with composition  $MFe_2O_4$  ( $M = Mn, Fe, Co$ ) synthesized by the thermal decomposition of metal-oleate precursors can be easily tuned while maintaining narrow size distribution; however, the initial as-synthesized state does not make the material particularly suitable for remote heating applications due to its low  $M_s$ .

In contrast, thermal decomposition of metal acetylacetonate precursors produces monodisperse  $MFe_2O_4$  MNPs with  $M_s$  comparable to bulk values in the as-synthesized state (**Table 1**). As expected, the saturation magnetization of  $CoFe_2O_4$  and  $MnFe_2O_4$  MNPs increases with increasing MNP diameter reaching 63 and 95  $emu\ g^{-1}$  for  $CoFe_2O_4$  and  $MnFe_2O_4$  respectively above 10 nm. Hysteresis loops of the  $MnFe_2O_4$  MNPs, 11 nm in diameter, measured at 5 K indicate a low coercive field of 250 Oe with no evidence of exchange bias (**Figure 5B**).  $CoFe_2O_4$  MNPs display a markedly higher coercivity of 20 kOe with no exchange bias. A dip in  $M_s$  to 28  $emu\ g^{-1}$  is measured for the 16 nm  $MnFe_2O_4$  MNPs. This may be attributed to the strong reducing environment of excess oleylamine, which was employed to increase the MNP diameter beyond 11 nm.<sup>35</sup> MNPs of  $MnFe_2O_4$  with diameters of 26 nm synthesized *via* our one-step heterogeneous nucleation exhibits the highest measured  $M_s$  (95  $emu\ g^{-1}$ ) in the synthesized MNP set due to its increase in volume to surface area ratio.

The tertiary ferrite MNPs synthesized from metal acetylacetonate precursors exhibit saturation behavior at high fields,  $M_s$  values comparable to those of bulk, and no evidence of exchange bias.

Because the synthesis involves a mixture of oleic acid, oleylamine, and 1,2-hexadecanediol with different reducing and oxidizing capabilities,<sup>35,37</sup> the reaction conditions may favor mixed valence states required for optimal magnetic properties of the ferrites. On the other hand, the thermal decomposition of metal-oleate precursors only requires the addition of oleic acid and the reaction conditions may not be sufficiently oxidizing to form ferrimagnetic spinel phases.

### **High Temperature Phase Transfer of MNPs into Aqueous Solutions**

While high temperature thermolysis of organometallic precursors produces monodisperse MNPs with controllable shape and size, the surface is generally coated with hydrophobic ligands, which make them unusable for biological applications in aqueous environments. To render the nanocrystals hydrophilic, we employ high-temperature phase transfer in diethylene glycol, a high boiling point polar solvent miscible with organic solvents such as toluene, to drive the coordination of polyacrylic acid (PAA) onto the surface of the MNPs at temperatures greater than 200 °C.<sup>38</sup> This strategy is advantageous because the high temperature promotes the exchange of the original surfactant with the polyelectrolyte through mass action. Furthermore, the multiple binding sites prevent PAA desorption, while allowing its extension into water to make the nanocrystals highly soluble in aqueous media. Ligand exchange with PAA resulted in the MNPs to be highly stable in Good's buffers such as tris(hydroxymethyl)aminomethane (Tris) and (4-(2-hydroxyethyl)-1-piperazineethanesulfonic acid ) (HEPES), although time-dependent aggregation was observed in phosphate buffered saline (PBS) which has been attributed to the formation of salt bridges (**Figure S5**).<sup>39</sup>

Interestingly, we find that the magnetic properties of the MNPs prepared by the thermal decomposition of metal-oleate precursors are significantly improved during the phase transfer process. For iron oxide MNPs,  $M_s$  values increase from 15 - 40 emu g<sup>-1</sup> to an average of 67 emu



$\text{g}^{-1}$ , which is comparable to bulk values of magnetite ( $92 \text{ emu g}^{-1}$ , **Figure 4A**). Furthermore, the coercive field decreases from 1350 to 350 Oe and there is no observable exchange bias (**Figure 5C**). The magnetic diameters are also found to correlate closely with the physical MNP diameters determined by TEM, and the ferromagnetic volume fraction exceeds 60% (**Table 1**). These improvements in the magnetic properties can be attributed to the conversion of the wüstite phase into a ferrimagnetic spinel phase. The high temperature phase transfer step provides an oxidizing environment that enables the transformation of metastable wüstite into maghemite and magnetite phases, with no evidence of FeO peaks apparent in the powder diffraction pattern (**Figure 6B**). Our data are in agreement with prior reports that observe the conversion of wüstite MNPs into  $\text{Fe}_3\text{O}_4$  and  $\gamma\text{-Fe}_2\text{O}_4$  during annealing in air at temperatures between  $140 - 200 \text{ }^\circ\text{C}$ .<sup>35</sup>

The  $M_s$  values of the  $\text{MnFe}_2\text{O}_4$  and  $\text{CoFe}_2\text{O}_4$  MNPs synthesized from metal-oleate precursors improves dramatically by 4-10 times, however their extremely low starting values still impede the application of these MNPs for efficient heat dissipation (**Table 1**). The magnetic properties of the MNPs synthesized from the metal-acac precursors are preserved during the phase transfer (**Figure 5D**). Furthermore, the ferromagnetic volume fraction for  $\text{MnFe}_2\text{O}_4$  MNPs is found to exceed 80% (**Table 1**). These observations also support our initial treatment of iron oxide and  $\text{MnFe}_2\text{O}_4$  MNPs as having uniaxial anisotropy because the remanent to saturation magnetization ratio is calculated to be less than 0.5 from the SQUID hysteresis curves, while the value calculated for  $\text{CoFe}_2\text{O}_4$  MNPs is 0.84 and suggests cubic anisotropy.<sup>18</sup>

### **Measurements of the Specific Loss Power**

To experimentally verify the predictive capabilities of the numerical calculations, heat dissipation of the MNPs dispersed in water is measured during exposure to an AMF produced by a home-made coil with a soft ferromagnetic toroid core driven by a RLC circuit. MNP solutions

(2 mg/mL) in water are placed into an AMF of amplitude  $H_0 = 15.5 \pm 1.4 \text{ kA m}^{-1}$  and frequency  $f = 500 \text{ kHz}$ . The temperature increase is recorded as a function of time, and the SLP is calculated from the slope using the expression:

$$SLP = \frac{C}{m} \frac{dT}{dt}$$

where  $C$  is the specific heat capacity of water per unit volume ( $C = 4.184 \text{ J K}^{-1} \text{ mL}^{-1}$ ),  $m$  is the concentration (g/mL of the ferrofluid), and  $\frac{dT}{dt}$  is the experimentally measured slope of the temperature increase as a function of time inside the AMF. The resulting SLP values are plotted in **Figure 7** as a function of MNP size.

The trends simulated in **Figure 1B** are qualitatively reproduced in the experimental measurements illustrated in **Figure 7**.  $\text{CoFe}_2\text{O}_4$  MNPs from both oleate and acac-based syntheses do not yield significant hysteretic losses under the given AMF parameters, and the observed heat dissipation originates from their Brownian rotation.<sup>15</sup> In the case of  $\text{MnFe}_2\text{O}_4$  with comparatively low  $K_{eff}$  values, the small magnitude of the anisotropy energy barrier of the MNPs smaller than 22 nm in diameter relative to the thermal energy at room temperature results in superparamagnetic like behavior, with little or no observable hysteretic loss. Only MNPs with diameters of 26 nm exhibit significant heating. For materials with intermediate anisotropy energies such as iron oxide, an optimal size range between 18 – 22 nm is identified for the applied AMF parameters. The SLP value of iron oxide MNPs 22 nm in diameter was measured to be  $716 \pm 31 \text{ W g}^{-1}$ , which is among the highest recorded values for synthetic ferrite materials at the given frequency and field strength.<sup>40</sup> This behavior is consistent with the calculated areas of the hysteresis loops in **Figure 1A**, which increase progressively due to a transition from reversible superparamagnetic to ferromagnetic hysteresis loss regimes.

Also of note is the difference in SLP between tertiary ferrite MNPs prepared from the two different synthetic routes. MNPs prepared from the metal-oleate precursors have lower measured SLP values compared to similar sized MNPs prepared from metal acetylacetonate precursors consistent with their lower magnetization at a given AMF amplitude. For example, 11 nm  $\text{MnFe}_2\text{O}_4$  MNPs prepared from acac precursors have SLP values of  $35 \text{ W g}^{-1}$  while MNPs prepared from oleate precursors have SLP values of  $13 \text{ W g}^{-1}$ . Furthermore, their low ferromagnetic volume fraction leads to deviations from numerical simulations as seen in the measured SLP value of  $44 \text{ W g}^{-1}$  for 28 nm MNPs prepared from oleate precursors. In contrast,  $\text{MnFe}_2\text{O}_4$  MNPs prepared from acetylacetonate chemistries trend with predictions due to their optimized magnetic properties, with a measured SLP of  $304 \text{ W g}^{-1}$ .

In summary, we find that tuning of the MNP diameter using thermal decomposition of metal-oleate precursors can be accomplished by simply changing the final reaction temperature, while monodispersity can be achieved with slow heating rates. Furthermore, the magnetic properties of the MNPs produced by this method can be significantly improved by annealing at high temperatures during the ligand transfer step, which results in the conversion of the antiferromagnetic wüstite phase present in the as-synthesized MNPs into a ferrimagnetic mixed spinel phase necessary for efficient hysteretic heat dissipation. In addition to metal-oleate based synthesis, we have explored metal-acac based synthesis, which requires the use of ligands with different reducing capabilities, to produce MNPs with saturation magnetization values approaching bulk. While previous reports of metal-acac synthesis have employed incremental coating of  $\sim 1$  nm layers to produce MNP diameters above 10 nm, our synthetic route allows for a one-step growth of 5-7 nm thick shells, which produces high-quality  $\text{MFe}_2\text{O}_4$  MNPs with diameters of up to 26 nm. All our MNPs are made soluble in aqueous environments and are

stable in physiological buffers for several months. These stable aqueous dispersions were subjected to an applied alternating magnetic field and their hysteretic power loss properties were compared to the simulated trends illustrating the predictive ability of the coherent magnetization reversal model. When the properties of the MNPs were not optimal, poor correlation with simulation was observed. Using our synthetic procedures we achieved some of the highest heating rates measured with 22 nm iron oxide MNPs at the specified magnetic field conditions.

## **CONCLUSION**

In this article, the domain of applicability of coherent magnetization reversal model in single-domain MNPs is generalized to field amplitudes and frequencies relevant to magnetic hyperthermia, and heat dissipation is evidently correlated to the anisotropy energy of the material. Within a framework of this model a suit of synthetic procedures is developed to produce water-soluble MNPs with magnetocrystalline anisotropy energy varying over 3 orders of magnitude in gram-scale quantities (**Figure S3**).

While magnetic hyperthermia for cancer applications has benefitted from decades of research, recent studies have demonstrated the use of hysteretic heat dissipation by MNPs for biomedical treatments beyond tumor necrosis. These innovative applications, such as the remote control of action potential firing in neurons, demand MNPs with optimized magnetic properties to achieve therapeutic effects at biologically relevant timescales. Thorough understanding and tailoring of the magnetocrystalline anisotropy energy and the saturation magnetization of the MNPs at a given field amplitude and frequency allows for control over the hysteretic heat dissipation critical for these biomedical applications. Equipped with a large-scale reproducible synthetic toolbox and a clearer understanding of MNP heat dissipation in the presence of an AMF, we can now begin to standardize hyperthermia treatments by selecting materials with the proper

anisotropy energy relevant for a particular therapeutic application. Tailoring hysteretic power loss will enable precise control over local temperature changes at cell surfaces decorated with MNPs, and may allow for fine temporal control over cellular functions.

## MATERIALS AND METHODS

Sodium oleate was purchased from TCI America. All other solvents and reagents were purchased from Sigma-Aldrich and used without further purification.

**Preparation of metal-oleate complex.** The metal-oleate  $MFe_2(C_{18}H_{33}O_2)_8$  precursor (where M = Fe, Co, Mn) was prepared by reacting sodium oleate and the respective metal chloride salt.<sup>19,21</sup>

We scaled our preparation such that the total metal content was 60 mmol per reaction. For example, an iron-cobalt metal complex  $CoFe_2(C_{18}H_{33}O_2)_8$  was prepared by dissolving 40 mmol of  $FeCl_3$ , 20 mmol of  $CoCl_2$ , and 160 mmol of sodium oleate in 100 mL of ethanol, 100 mL of MilliQ water, and 200 mL of hexane and heated to reflux at 60 °C for 4 hours. After removal of the aqueous phase, the organic phase was heated to 70 °C for 2 hours and then placed under vacuum at 110 °C for an additional 2 hours to remove residual solvent, leaving behind a viscous metal-oleate product.

**Synthesis of monodisperse and spherical  $MFe_2O_4$  nanocrystals of different sizes from metal-oleate precursors.** To synthesize 15 nm in diameter iron oxide nanoparticles, 5 mmol of the metal-oleate complex and 2.5 mmol of oleic acid was dissolved in 25 mL of 1-octadecene in a 250 mL 3-neck flask and evacuated for 30 minutes. Then the solution was heated to 200 °C under nitrogen flow and further heated to 310 °C at a rate of 1 °C/min and held at the specified temperature for 1 hour. After removing the heating mantle and cooling to room temperature, an entire reaction solution was transferred into a 50 mL conical tube along with a 1:1 mixture of ethanol and hexane. The sample was centrifuged at 6000 rpm for 10 minutes to collect the synthesized nanocrystals. The pelleted nanocrystals were redispersed in 10 mL of hexane and flocculated with 5 mL of ethanol and centrifuged at 6000 rpm for 10 minutes twice to remove

excess ligand and solvent. The nanocrystals were then dispersed in toluene after. 10 nm, 18 nm, and 23 nm MNPs were synthesized by setting the final temperature to 305 °C, 320 °C, and 325 °C respectively. 26 nm MNPs were prepared by setting the final temperature to 330 °C in 25 mL of 1-eicosene.

To synthesize  $\text{MnFe}_2\text{O}_4$  15 nm MNPs, 5 mmol of the metal-oleate complex and 2.5 mmol of oleic acid was dissolved in 10 mL of 1-octadecene in a 250 mL 3-neck flask and evacuated for 30 minutes. Then the solution was heated to 200 °C under nitrogen flow and further heated to 315 °C at a rate of 1 °C/min and held at the specified temperature for 1 hour. 10 nm and 18 nm MNPs were synthesized by setting the final temperature to 305 °C and 325 °C respectively. 28 nm MNPs were prepared by setting the final temperature to 330 °C in 10 mL of 1-eicosene.

To synthesize  $\text{CoFe}_2\text{O}_4$  13 nm MNPs, 5 mmol of the metal-oleate complex and 2.5 mmol of oleic acid was dissolved in 25 mL of 1-octadecene in a 250 mL 3-neck flask and evacuated for 30 minutes. Then the solution was heated to 200 °C under nitrogen flow and further heated to 305 °C at a rate of 1 °C/min and held at the specified temperature for 1 hour. 20 nm MNPs were preparing by setting the final temperature to 310 °C with a change in heating rate from 1 °C/min to 3 °C/min.

**Synthesis of monodisperse  $\text{MnFe}_2\text{O}_4$  nanocrystals of different sizes from metal acetylacetonate (acac) precursors.** 7 nm  $\text{MnFe}_2\text{O}_4$  MNPs were synthesized by previously reported methods in a 250 mL 3-neck flask.<sup>20</sup> To increase the size of the MNPs,  $\text{MnCl}_2$  instead of  $\text{Mn}(\text{acac})_2$  was used. 11 nm MNPs were synthesized by mixing  $\text{Fe}(\text{acac})_3$  (2 mmol),  $\text{MnCl}_2$  (1 mmol), oleic acid (6 mmol), oleylamine (6 mmol), 1,2-hexadecanediol (10 mmol), and 20 mL of benzyl ether and evacuated for 30 minutes. Then the solution was heated to reflux for one hour

at a rate of 3.3 °C/min under nitrogen flow. MNPs 16 nm in diameter were synthesized by mixing Fe(acac)<sub>3</sub> (2 mmol), MnCl<sub>2</sub> (1 mmol), oleic acid (6.31 mmol), oleylamine (12.16 mmol), and 2 mL of dioctyl ether and heated to 200 °C under nitrogen flow for 2 hours. The reaction was further heated to 330 °C at a rate of 3.3 °C/min. To grow MnFe<sub>2</sub>O<sub>4</sub> MNPs greater than 20 nm, 50 mg of 11 nm MNP seeds dispersed in hexane was added to Fe(acac)<sub>3</sub> (2 mmol), MnCl<sub>2</sub> (1 mmol), oleic acid (6 mmol), oleylamine (6 mmol), 1,2-hexadecanediol (10 mmol), and 20 mL of benzyl ether and evacuated for 30 minutes at 60 °C. Then the solution was heated to reflux for one hour at a rate of 3.3 °C/min under nitrogen flow.

9 nm CoFe<sub>2</sub>O<sub>4</sub> MNPs were synthesized by previously reported methods in a 250 mL 3-neck flask.<sup>20</sup> To increase the size of the nanoparticles, MnCl<sub>2</sub> instead of Mn(acac)<sub>2</sub> was used. 11 nm MNPs were synthesized by mixing Fe(acac)<sub>3</sub> (2 mmol), CoCl<sub>2</sub> (1 mmol), oleic acid (6 mmol), oleylamine (6 mmol), 1,2-hexadecanediol (10 mmol), and 20 mL of benzyl ether and evacuated for 30 minutes. Then the solution was heated to reflux for one hour at a rate of 3.3 °C/min under nitrogen flow.

**Phase Transfer.** The MNPs were transferred into water using a protocol adopted from Zhang *et al.*<sup>38</sup> 0.5 g of poly(acrylic acid) ( $M_w \sim 1800$ ) was dissolved in 10 mL diethylene glycol and heated to 110 °C under nitrogen. 1 mL of MNPs dispersed in hexane (~50 mg/mL) was injected into the mixture and then heated to reflux at 240 °C for 3 hours. The sample was precipitated with 10 mL of 1 M HCl then washed twice with water. 50 mM NaOH solution was added to disperse the MNPs and sonicated for 30 minutes.



Previously reported studies from the thermal decomposition of iron oleate indicate a yield of greater than 95%, although the method to quantify this was not reported. Based on the total MNP weight after removing organic matter by annealing at 400 °C for 4 hours, we obtain a yield of ~70 % per synthesis based on the molarity of iron from the nanoparticles to the amount contained in the precursor (~300 mg of as-synthesized MNPs per reaction). Similarly, the yield of MNPs from the thermal decomposition of iron acac precursors is ~60% and is typical of that reported (~80 mg of as synthesized MNPs per reaction). ~40% of the MNPs are lost upon phase transfer into water. To obtain ~1 g of water soluble MNPs, we scaled up the synthesis by 7 times and dispersed the MNPs after phase transfer scaled by 10 times into phosphate buffered saline (PBS) at a final concentration of 1 mg/mL.

**Transmission Electron Microscopy (TEM).** As-synthesized MNPs dispersed in hexane were drop casted onto carbon-coated copper grids (Ted Pella Inc.) and washed three times with methanol. TEM images were taken using a JEOL 2010F electron microscope at 200 kV.

**Elemental analysis.** Inductively coupled plasma atomic emission spectroscopy (ICP-AES) was used to determine the concentration of the transition metal ions on a Horiba ACTIVA-S. To remove residual ligands that may interfere with the degradation of MNPs in aqua regia, we annealed the samples in air at 400 °C for 4 hours. Organic ligands are expected to be fully decomposed above 350 °C. The amount of magnetic material in a given volume of 100 µL was determined by ICP-AES after annealing then digesting in a solution of aqua regia (1:3 v/v 37 wt % HCl to 70 wt % HNO<sub>3</sub>) overnight at 60 °C. The quantity of metal determined was used to normalize all magnetization and SLP values that were experimentally obtained.

**Magnetic Characterization.** MNPs in the as-synthesized state was dispersed in toluene and sealed in quartz tubes using rubber stoppers. Similarly for water-soluble MNPs, measurements were conducted with the sample dispersed in water. Hysteresis curves at 5 °K were measured using a superconducting quantum interference device (SQUID, MPMS-XL, Quantum Design). Room temperature hysteresis curves were generated on a vibrating sample magnetometer (VSM, Digital Measurement Systems Model 880A).

**Powder X-ray Diffraction.** Powder XRD diffraction patterns were collected with a PANalytical Multipurpose Diffractometer equipped with Cu K $\alpha$  radiation in the  $2\theta$  range of 20-80°. Samples were prepared from evaporating successive casting of dispersed MNPs onto glass.

**Stability Test.** 0.1 mg of MNPs as determined by [Fe] content was dispersed in either 1X Tris base, acetic acid and EDTA (TAE), HEPES, or 1X phosphate buffer saline (PBS) buffer for one month and its hydrodynamic diameter was compared to the same MNPs dispersed in MilliQ water using dynamic light scattering (DLS, Malvern Nano ZS90).

**Specific loss power measurements.** Calorimetry measurements in the presence of an AMF were conducted with a custom built setup. A toroid composed of a soft ferromagnetic material optimized for high frequency power transformers was specially machined to include a gap large enough to accommodate a sample vial and used as a coil core. A transformer circuit with a resistive ballast in the primary circuit was used to generate high, reasonably stable currents in the secondary while simultaneously matching the impedance of the variable frequency 200W

amplifier (1020L, Electronics & Innovation). In the secondary, the coil acted as the resistive and inductive elements of an RLC resonance circuit, with a high voltage series capacitor setting the resonant frequency. The field magnitude was measured by a custom built probe employing a pickup loop and an oscilloscope (TDS2022C, Tektronix). Error bars placed on the field value result primarily from the moderate heating of the core over the course of 30 seconds, which was mitigated by a simple cooling system circulating ice water to the coil *via* silicone tubing.

Temperature measurements made by an AMF insensitive fiber optic temperature probe were recorded as an AMF was applied for 30 seconds. Each measurement was repeated 8 times and control samples with only water were measured after every 4 trials to determine the background heating rate. All samples were 1 mL with a MNP concentration of approximately 2 mg/mL. The SLP value measured was normalized to the metal content determined by elemental analysis.

## **ACKNOWLEDGMENT**

This work was supported in part by the Sanofi Biomedical Innovation Award and the MRSEC Program of the National Science Foundation under award number DMR-0819762. RC is supported by the National Science Foundation Graduate Research Fellowship. Authors thank X. Jia for her advice on transmission electron microscopy, D. C. Bono on his assistance with vibrating sample magnetometry, M. F. Rubner and C. A. Ross for their insightful comments on the manuscript. PA and RC designed the study. RC and MGC performed experiments and simulations. RC, MGC and PA wrote the manuscript. All authors have given approval to the final version of the manuscript.

## **SUPPORTING INFORMATION AVAILABLE**

Additional experimental details and figures. This material is available free of charge *via* the Internet at <http://pubs.acs.org>.

## **ABBREVIATIONS**

MNP, magnetic nanoparticle; AMF, alternating magnetic field; SLP, specific loss power;  $M_s$ , saturation magnetization;  $K_{eff}$ , uniaxial anisotropy energy constant; LRT, linear response theory; acac, acetylacetonate.

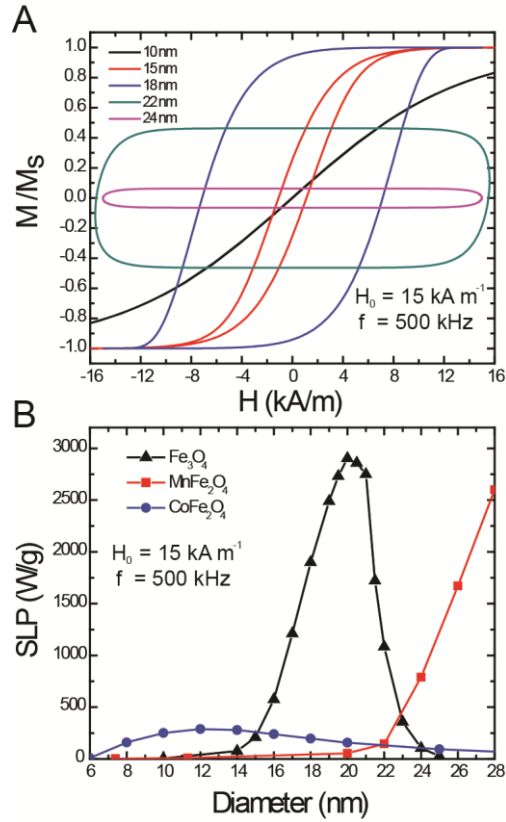


**Figure 1.** SLP calculations based on a physical model. (A) Field-dependent magnetization curves from numerical simulations for  $\text{Fe}_3\text{O}_4$  MNPs of diameters varying between 10-24 nm. (B) SLP determined by integrating the area of hysteresis loops for  $\text{Fe}_3\text{O}_4$ ,  $\text{MnFe}_2\text{O}_4$ , and  $\text{CoFe}_2\text{O}_4$  as a function of MNP diameter. Field parameters used were  $H_0 = 15 \text{ kA m}^{-1}$  and  $f = 500 \text{ kHz}$ .

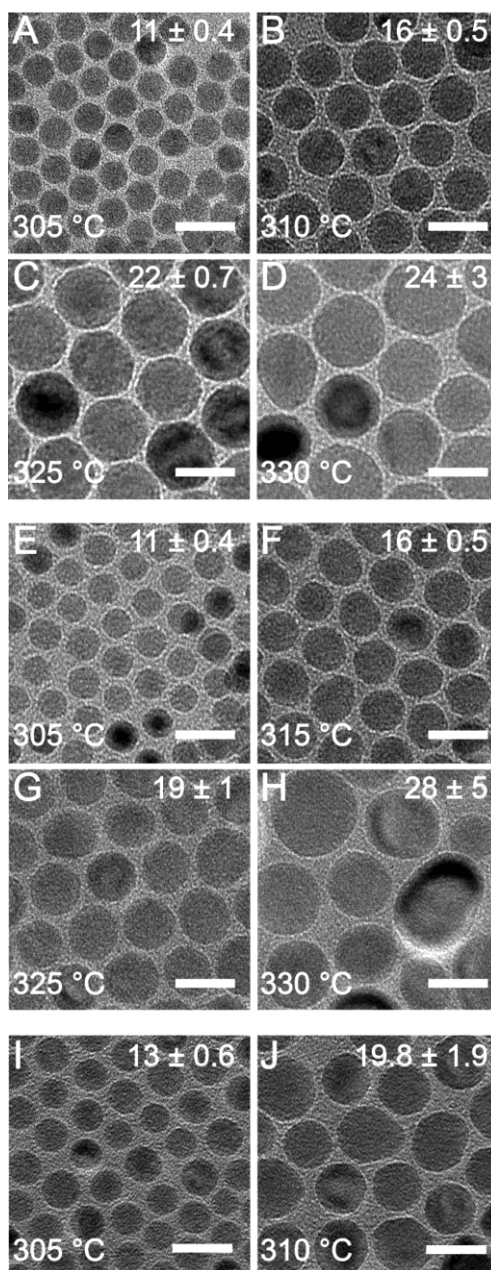


**Figure 2.** Transmission electron microscopy (TEM) images of MNPs synthesized *via* the thermal decomposition of metal-oleate precursors. The diameter, the standard deviation (nm) and the synthesis temperature are indicated on the images. (A-D) Iron oxide MNPs synthesized at 305, 310, 325 °C in octadecene yielding 11 nm, 16 nm, and 22 nm diameter MNPs respectively. 24 nm MNPs were synthesized at 330 °C in eicosane. (E-H) Manganese ferrite

MNPs synthesized at 305, 315, 325 °C in octadecene yielding 11 nm, 16 nm, and 19 nm diameter MNPs respectively. 28 nm MNPs were synthesized at 330 °C in eicosane. (I,J) 13 nm cobalt ferrite MNPs synthesized at 305°C. For 20 nm particles, the heating rate was increased to 3.3 °C/min to 310 °C. Scale bar = 20 nm.

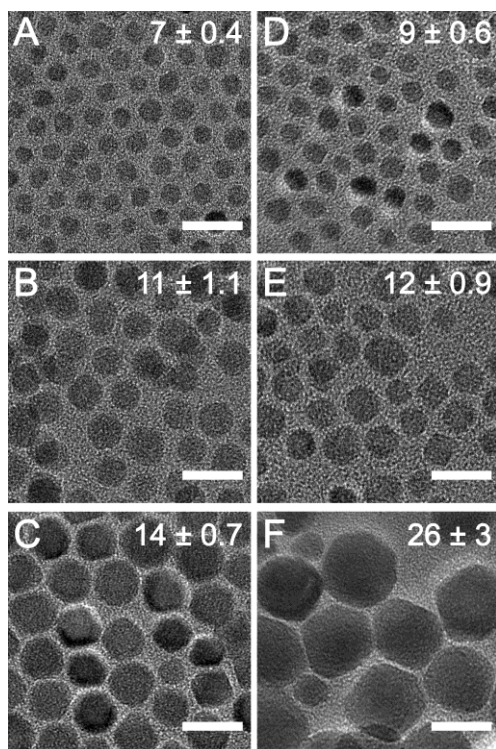


**Figure 3.** TEM images of  $MFe_2O_4$  MNPs synthesized from the thermal decomposition of metal acetylacetonate (acac) precursors. The size and the standard deviation (nm) are indicated on the images. (A - C) Cobalt ferrite MNPs with diameters of 9, 12, and 14 nm. (D - F) Manganese ferrite MNPs with diameters 7, 11, and 26 nm. Scale bar = 20 nm.



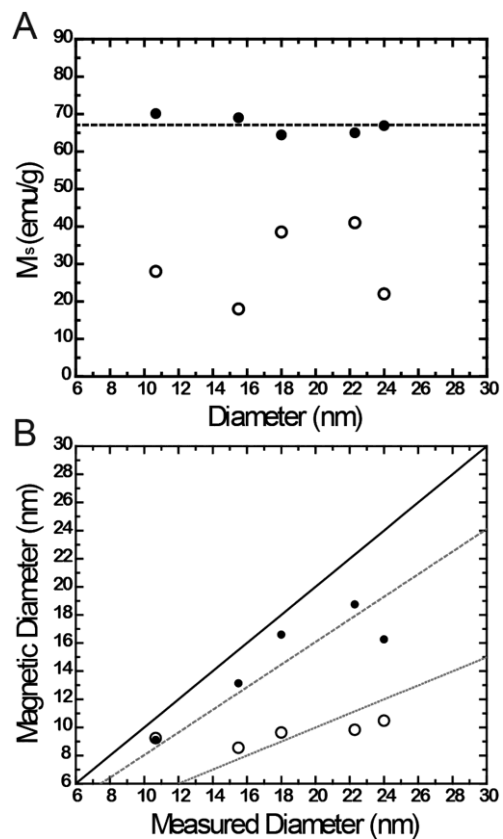


**Figure 4.** Magnetic properties of iron oxide MNPs in the as-synthesized (open circles) and water-soluble state (filled-in circles). (A)  $M_s$  increases after high-temperature annealing in phase-transfer step (B) Increase in magnetic diameter trending linearly with increasing MNP size. Solid black line represents 1:1 correspondence, grey dashed-lines are from linear fits to the data with intercept set at 0.

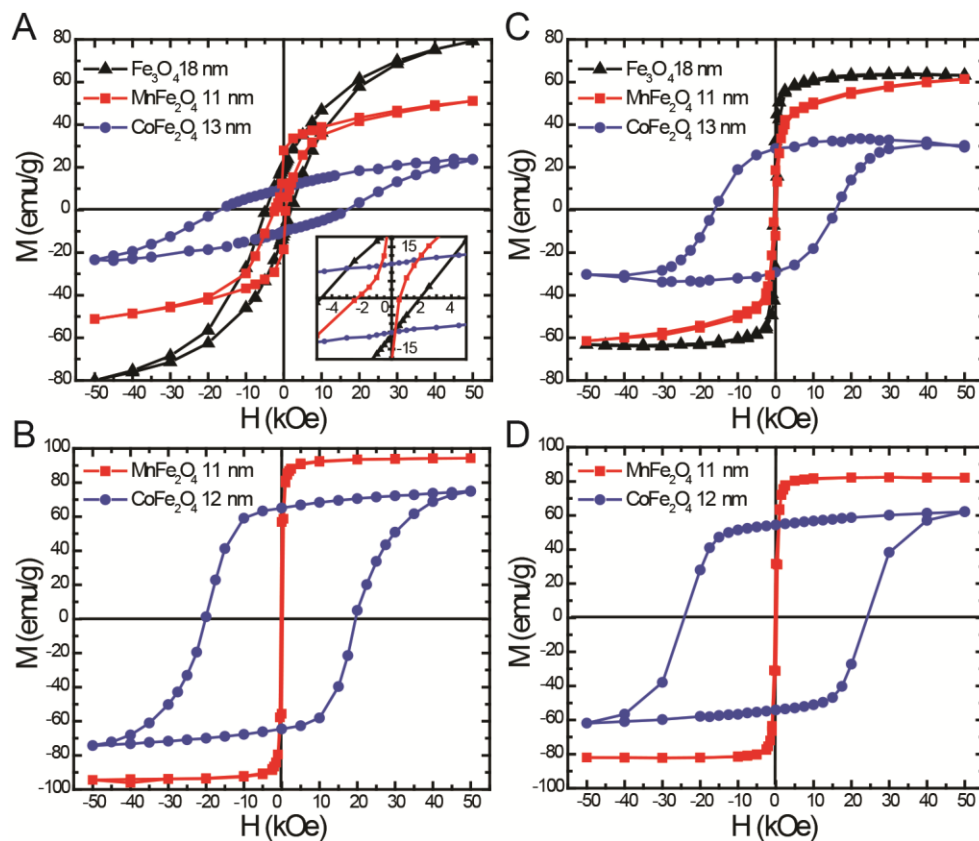


**Figure 5.** Field-dependent magnetization loops for tertiary ferrites measured at 5 °K. (A) As-synthesized MNPs from thermal decomposition of metal-oleate precursors. Inset: low-field region shows negative field shift characteristic of exchange bias. (B) As-synthesized MNPs from thermal decomposition of metal-acac precursors. (C) MNPs from metal-oleate synthesis in (A) after phase transfer into water. (D) MNPs from metal-acac synthesis in (B) after phase transfer into water.

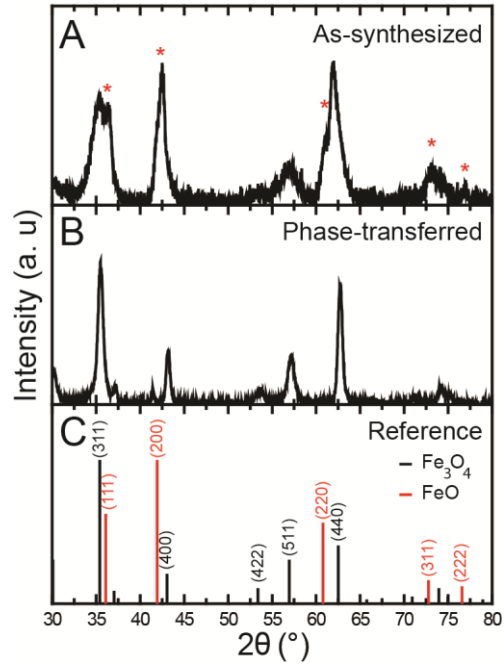


**Figure 6.** Powder x-ray diffraction patterns of (A) as-synthesized iron oxide nanoparticles with the wüstite FeO phase marked with a red asterisk, and (B) after phase-transfer into water. (C) Reference pattern of bulk Fe<sub>3</sub>O<sub>4</sub> (black) and FeO (red).

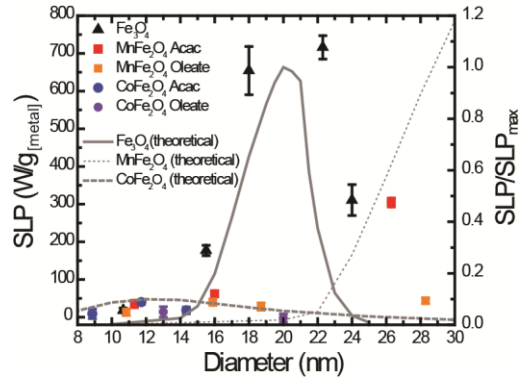


**Figure 7.** SLP measurements as a function of NP size (measured by TEM) obtained at  $H_0 = 15.5 \pm 1.4 \text{ kA m}^{-1}$  and  $f = 500 \text{ kHz}$ . The calculations based on theoretical models are normalized to the maximum SLP value calculated for 20 nm iron oxide MNPs, and the experimental SLP are normalized to the metal content determined from elemental analysis.

**Table 1.** Summary of Magnetic Properties of as-synthesized and water-soluble MNPs at 300K.<sup>a</sup>

Sample	d (nm)	d <sub>mag</sub> (nm)	d* <sub>mag</sub> (nm)	M <sub>s</sub> (300K) (emu/g)	M <sub>s</sub> * (300K) (emu/g)	Φ <sub>Ferrimagnetic</sub>
Iron Oxide Oleate	11	9.2	9.1	28	70	0.58 (0.56)
	16	8.5	13.1	18	69	0.15 (0.55)
	18	9.6	16.6	39	64	0.15 (0.78)
	22	9.8	18.8	41	65	0.09 (0.62)
	24	10.5	16.3	22	67	0.08 (0.31)
MnFe <sub>2</sub> O <sub>4</sub>	11	7.7	7.6	8	47	0.34 (0.33)
Oleate	16	10.8	10.2	13	54	0.31 (0.26)
	19	9.8	9.6	5	25	0.14 (0.13)
	28	9.0	11.4	3	31	0.03 (0.07)
CoFe <sub>2</sub> O <sub>4</sub>	13			15.2	30.8	
Oleate	20			3	7	
MnFe <sub>2</sub> O <sub>4</sub>	7	6.6	6.5	53	51	0.84 (0.80)
Acac	11	9.2	10.6	75	74	0.58 (0.89)
	26	10.9	25.3	86	92	0.07 (0.92)
CoFe <sub>2</sub> O <sub>4</sub>	9			39	37	
Acac	12			60	62	
	14			58	59	

<sup>a</sup>Average diameters (d) were extracted from TEM images. Magnetic diameters (d<sub>mag</sub>) were obtained from linear fits of root temperature hysteresis curves in the low field range. \*Indicates the sample was measured from water-soluble MNP solutions. The Φ<sub>Ferrimagnetic</sub> indicates the volume fraction that is ferromagnetic. The bracketed values indicate the volume fraction after phase transfer into water.



## REFERENCES

- (1) Lu, A. H.; Salabas, E. e. L.; Schüth, F. Magnetic Nanoparticles: Synthesis, Protection, Functionalization, and Application. *Angew. Chem., Int. Ed.* **2007**, *46*, 1222-1244.
- (2) Mornet, S.; Vasseur, S.; Grasset, F.; Duguet, E. Magnetic Nanoparticle Design for Medical Diagnosis and Therapy. *J. Mater. Chem.* **2004**, *14*, 2161-2175.
- (3) Cullity, B. D.; Graham, C. D. *Introduction to Magnetic Materials*; Wiley-IEEE Press, 2011.
- (4) Jang, J.; Nah, H.; Lee, J.; Moon, S. H.; Kim, M. G.; Cheon, J. Critical Enhancements of MRI Contrast and Hyperthermic Effects by Dopant-Controlled Magnetic Nanoparticles. *Angew. Chem., Int. Ed.* **2009**, *48*, 1234-1238.
- (5) Lee, J.; Jang, J.; Choi, J.; Moon, S. H.; Noh, S.; Kim, J.; Kim, J.; Kim, I.; Park, K. I.; Cheon, J. Exchange-coupled Magnetic Nanoparticles for Efficient Heat Induction. *Nat Nano* **2011**, *6*, 418-422.
- (6) Maaz, K.; Mumtaz, A.; Hasanain, S. K.; Ceylan, A. Synthesis and Magnetic Properties of Cobalt Ferrite (CoFe<sub>2</sub>O<sub>4</sub>) Nanoparticles Prepared by Wet Chemical Route. *J. Magn. Magn. Mater.* **2007**, *308*, 289-295.
- (7) Huang, H.; Delikanli, S.; Zeng, H.; Ferkey, D. M.; Pralle, A. Remote Control of Ion Channels and Neurons through Magnetic-Field Heating of Nanoparticles. *Nat Nano* **2010**, *5*, 602-606.
- (8) Stanley, S. A.; Gagner, J. E.; Damanpour, S.; Yoshida, M.; Dordick, J. S.; Friedman, J. M. Radio-Wave Heating of Iron Oxide Nanoparticles Can Regulate Plasma Glucose in Mice. *Science* **2012**, *336*, 604-608.

- (9) Hergt, R.; Dutz, S. Magnetic Particle Hyperthermia—Biophysical Limitations of a Visionary Tumour Therapy. *J. Magn. Magn. Mater.* **2007**, *311*, 187-192.
- (10) Carrey, J.; Mehdaoui, B.; Respaud, M. Simple Models for Dynamic Hysteresis Loop Calculations of Magnetic Single-domain Nanoparticles: Application to Magnetic Hyperthermia Optimization. *J. Appl. Phys.* **2011**, *109*, 083921-083917.
- (11) Mehdaoui, B.; Meffre, A.; Carrey, J.; Lachaize, S.; Lacroix, L.-M.; Gougeon, M.; Chaudret, B.; Respaud, M. Optimal Size of Nanoparticles for Magnetic Hyperthermia: A Combined Theoretical and Experimental Study. *Adv. Funct. Mater.* **2011**, *21*, 4573-4581.
- (12) Kodama, R. H. Magnetic Nanoparticles. *J. Magn. Magn. Mater.* **1999**, *200*, 359-372.
- (13) Yoon, S.; Krishnan, K. M. Temperature Dependence of Magnetic Anisotropy Constant in Manganese Ferrite Nanoparticles at Low Temperature. *J. Appl. Phys.* **2011**, *109*, 07B534-533.
- (14) Rosensweig, R. E. Heating Magnetic Fluid with Alternating Magnetic Field. *J. Magn. Magn. Mater.* **2002**, *252*, 370-374.
- (15) Fortin, J.; Wilhelm, C.; Servais, J.; Ménager, C.; Bacri, J.; Gazeau, F. Size-Sorted Anionic Iron Oxide Nanomagnets as Colloidal Mediators for Magnetic Hyperthermia. *J. Am. Chem. Soc.* **2007**, *129*, 2628-2635.
- (16) Stoner, E. C.; Wohlfarth, E. P. A Mechanism of Magnetic Hysteresis in Heterogeneous Alloys. *Philosophical Transactions of the Royal Society of London. Series A. Mathematical and Physical Sciences* **1948**, 599-642.



- (17) Usov, N. A.; Grebenshchikov, Y. B. Hysteresis Loops of an Assembly of Superparamagnetic Nanoparticles with Uniaxial Anisotropy. *J. Appl. Phys.* **2009**, *106*, 023917-023911.
- (18) Ibusuki, T.; Kojima, S.; Kitakami, O.; Shimada, Y. Magnetic Anisotropy and Behaviors of Fe Nanoparticles. *Magnetics, IEEE Transactions on* **2001**, *37*, 2223-2225.
- (19) Bao, N.; Shen, L.; Wang, Y.; Padhan, P.; Gupta, A. A Facile Thermolysis Route to Monodisperse Ferrite Nanocrystals. *J. Am. Chem. Soc.* **2007**, *129*, 12374-12375.
- (20) Sun, S.; Zeng, H.; Robinson, D. B.; Raoux, S.; Rice, P. M.; Wang, S. X.; Li, G. Monodisperse MFe<sub>2</sub>O<sub>4</sub> (M = Fe, Co, Mn) Nanoparticles. *J. Am. Chem. Soc.* **2003**, *126*, 273-279.
- (21) Park, J.; An, K.; Hwang, Y.; Park, J.; Noh, H.; Kim, J.; Park, J.; Hwang, N.; Hyeon, T. Ultra-Large-Scale Syntheses of Monodisperse Nanocrystals. *Nat. Mater.* **2004**, *3*, 891-895.
- (22) Salas, G.; Casado, C.; Teran, F. J.; Miranda, R.; Serna, C. J.; Morales, M. P. Controlled Synthesis of Uniform Magnetite Nanocrystals with High-Quality Properties for Biomedical Applications. *J. Mater. Chem.* **2012**, *22*, 21065-21075.
- (23) Bronstein, L. M.; Huang, X.; Retrum, J.; Schmucker, A.; Pink, M.; Stein, B. D.; Dragnea, B. Influence of Iron Oleate Complex Structure on Iron Oxide Nanoparticle Formation. *Chem. Mater.* **2007**, *19*, 3624-3632.
- (24) Gheisari, M.; Mozaffari, M.; Acet, M.; Amighian, J. Preparation and Investigation of Magnetic Properties of Wüstite Nanoparticles. *J. Magn. Magn. Mater.* **2008**, *320*, 2618-2621.
- (25) Bao, N.; Shen, L.; An, W.; Padhan, P.; Heath Turner, C.; Gupta, A. Formation Mechanism and Shape Control of Monodisperse Magnetic CoFe<sub>2</sub>O<sub>4</sub> Nanocrystals. *Chem. Mater.* **2009**, *21*, 3458-3468.

- (26) Kwon, S. G.; Hyeon, T. Formation Mechanisms of Uniform Nanocrystals *via* Hot-Injection and Heat-Up Methods. *Small* **2011**, *7*, 2685-2702.
- (27) Song, Q.; Ding, Y.; Wang, Z. L.; Zhang, Z. J. Tuning the Thermal Stability of Molecular Precursors for the Nonhydrolytic Synthesis of Magnetic MnFe<sub>2</sub>O<sub>4</sub> Spinel Nanocrystals. *Chem. Mater.* **2007**, *19*, 4633-4638.
- (28) Xie, J.; Peng, S.; Brower, N.; Pourmand, N.; Wang, S. X.; Sun, S. One-Pot Synthesis of Monodisperse Iron Oxide Nanoparticles for Potential Biomedical Applications. *Pure Appl. Chem.* **2006**, *78*, 1003-1014.
- (29) Noh, S.; Na, W.; Jang, J.; Lee, J.; Lee, E. J.; Moon, S. H.; Lim, Y.; Shin, J.; Cheon, J. Nanoscale Magnetism Control *via* Surface and Exchange Anisotropy for Optimized Ferrimagnetic Hysteresis. *Nano Lett.* **2012**, *12*, 3716-3721.
- (30) Morales, M. P.; Veintemillas-Verdaguer, S.; Montero, M. I.; Serna, C. J.; Roig, A.; Casas, L.; Martínez, B.; Sandiumenge, F. Surface and Internal Spin Canting in  $\gamma$ -Fe<sub>2</sub>O<sub>3</sub> Nanoparticles. *Chem. Mater.* **1999**, *11*, 3058-3064.
- (31) Nogués, J.; Schuller, I. K. Exchange Bias. *J. Magn. Magn. Mater.* **1999**, *192*, 203-232.
- (32) Nogués, J.; Sort, J.; Langlais, V.; Skumryev, V.; Surinach, S.; Munoz, J. S.; Baró, M. D. Exchange Bias in Nanostructures. *Phys. Rep.* **2005**, *422*, 65-117.
- (33) Levy, M.; Quarta, A.; Espinosa, A.; Figuerola, A.; Wilhelm, C.; Garcia-Hernandez, M.; Genovese, A.; Falqui, A.; Alloyeau, D.; Buonsanti, R.; *et al.* Correlating Magneto-Structural Properties to Hyperthermia Performance of Highly Monodisperse Iron Oxide Nanoparticles Prepared by a Seeded-Growth Route. *Chem. Mater.* **2011**, *23*, 4170-4180.

- (34) Kavich, D. W.; Dickerson, J. H.; Mahajan, S. V.; Hasan, S. A.; Park, J. H. Exchange Bias of Singly Inverted FeO/Fe<sub>3</sub>O<sub>4</sub> Core-Shell Nanocrystals. *Phys. Rev. B* **2008**, *78*, 174414.
- (35) Hou, Y.; Xu, Z.; Sun, S. Controlled Synthesis and Chemical Conversions of FeO Nanoparticles. *Angew. Chem., Int. Ed.* **2007**, *46*, 6329-6332.
- (36) Casula, M. F.; Jun, Y.-w.; Zaziski, D. J.; Chan, E. M.; Corrias, A.; Alivisatos, A. P. The Concept of Delayed Nucleation in Nanocrystal Growth Demonstrated for the Case of Iron Oxide Nanodisks. *J. Am. Chem. Soc.* **2006**, *128*, 1675-1682.
- (37) Xu, Z.; Shen, C.; Hou, Y.; Gao, H.; Sun, S. Oleylamine as Both Reducing Agent and Stabilizer in a Facile Synthesis of Magnetite Nanoparticles. *Chem. Mater.* **2009**, *21*, 1778-1780.
- (38) Zhang, T.; Ge, J.; Hu, Y.; Yin, Y. A General Approach for Transferring Hydrophobic Nanocrystals into Water. *Nano Lett.* **2007**, *7*, 3203-3207.
- (39) Xu, Y.; Qin, Y.; Palchoudhury, S.; Bao, Y. Water-Soluble Iron Oxide Nanoparticles with High Stability and Selective Surface Functionality. *Langmuir* **2011**, *27*, 8990-8997.
- (40) Guardia, P.; Di Corato, R.; Lartigue, L.; Wilhelm, C.; Espinosa, A.; Garcia-Hernandez, M.; Gazeau, F.; Manna, L.; Pellegrino, T. Water-Soluble Iron Oxide Nanocubes with High Values of Specific Absorption Rate for Cancer Cell Hyperthermia Treatment. *ACS Nano* **2012**, *6*, 3080-3091.